frontiers | Frontiers in Cell and Developmental Biology

TYPE Original Research
PUBLISHED 23 June 2023
DOI 10.3389/fcell.2023.1126819

OPEN ACCESS

EDITED BY
Namrata Gundiah,
Indian Institute of Science (IISc), India

REVIEWED BY
Takashi Miura,
Kyushu University, Japan
Rui Travasso,
University of Coimbra, Portugal

*CORRESPONDENCE
Katsuhiko Sato,
katsuhiko_sato@es.hokudai.ac.jp

RECEIVED 19 December 2022
ACCEPTED 30 May 2023
PUBLISHED 23 June 2023

CITATION
Sato K (2023), A cell membrane model that reproduces cortical flow-driven cell migration and collective movement. *Front. Cell Dev. Biol.* 11:1126819. doi: 10.3389/fcell.2023.1126819

A cell membrane model that reproduces cortical flow-driven cell migration and collective movement

Katsuhiko Sato*

Research Institute for Electronic Science, Hokkaido University, Sapporo, Japan

Many fundamental biological processes are dependent on cellular migration. Although the mechanical mechanisms of single-cell migration are relatively well understood, those underlying migration of multiple cells adhered to each other in a cluster, referred to as cluster migration, are poorly understood. A key reason for this knowledge gap is that many forces—including contraction forces from actomyosin networks, hydrostatic pressure from the cytosol, frictional forces from the substrate, and forces from adjacent cells—contribute to cell cluster movement, making it challenging to model, and ultimately elucidate, the final result of these forces. This paper describes a two-dimensional cell membrane model that represents cells on a substrate with polygons and expresses various mechanical forces on the cell surface, keeping these forces balanced at all times by neglecting cell inertia. The model is discrete but equivalent to a continuous model if appropriate replacement rules for cell surface segments are chosen. When cells are given a polarity, expressed by a direction-dependent surface tension reflecting the location dependence of contraction and adhesion on a cell boundary, the cell surface begins to flow from front to rear as a result of force balance. This flow produces unidirectional cell movement, not only for a single cell but also for multiple cells in a cluster, with migration speeds that coincide with analytical results from a continuous model. Further, if the direction of cell polarity is tilted with respect to the cluster center, surface flow induces cell cluster rotation. The reason why this model moves while keeping force balance on cell surface (i.e., under no net forces from outside) is because of the implicit inflow and outflow of cell surface components through the inside of the cell. An analytical formula connecting cell migration speed and turnover rate of cell surface components is presented.

KEYWORDS

force balance, surface flow, cell cluster migration, cell cluster rotation, analytical formula for cell migration, mechanical model

1 Introduction

Cellular migration is a key component of numerous biological processes, including the morphogenesis of multicellular organisms, wound healing, and cancer metastasis (Friedl and Gilmour, 2009; Scarpa and Mayor, 2016; Bodor et al., 2020). Consequently, elucidating the molecular and biophysical mechanisms that control cell movement can provide fundamental insight to enhance our understanding of these critical processes. Notably, although the mechanisms controlling single-cell migration are relatively well understood (Bodor et al.,

2020), those underlying multiple-cell migration, wherein cells adhere to each other and form a cluster, prior to undergoing unidirectional (Haas and Gilmour, 2006; Weijer, 2009; Haigo and Bilder, 2011; Montell et al., 2012; Kuwayama and Ishida, 2013; Pagès et al., 2022) and rotational motion (Founounou et al., 2021), referred to as cluster migration, remain unclear. One reason for this is that the phenomenon of cluster migration involves what is known as a many-body problem. That is, within cells, there are many forces related to cell movement, such as contraction forces coming from actomyosin, adhesion forces between cells, hydrostatic pressure from cytosol, and forces from adjacent cells; cell movement is a result of balance between these forces. Thus, whereas it is challenging to determine how cell membranes move under this force balance even for a single cell, it is even more difficult in the case of multiple cells, particularly when trying to understand how multiple cells coordinately move. In such complex scenarios, mechanical modeling approaches may be useful, given that these methods guarantee force balance for every element and hence, generate results that can be relied upon with some conviction.

Cell movements are mainly classified into one of two types (Callan-Jones and Voituriez, 2016). In mesenchymal migration, the cell attaches to a substrate at focal adhesions and extends its body at the leading edge by forming lamellipodia and filopodia (Innocenti, 2018). During this process, a retrograde flow of actin filaments is observed beneath the plasma membrane of the cell (Haas and Gilmour, 2006; Case and Waterman, 2015). The second type of cell movement is amoeboid migration; in this case, specific adhesion to the substrate is not necessarily required, but, nonspecific friction between the cell membrane and the surrounding matrix is thought to be sufficient for migration (Lämmermann et al., 2008; Reversat et al., 2020; O'Neill et al., 2018; Farutin et al., 2019). By contracting the rear part of the cell body via a force generated from the actomyosin meshwork under the plasma membrane, the cell increases hydrostatic pressure within the cytosol and produces blebs at the leading edge to extend its body forward (Paluch and Raz, 2013). During ameboid migration, cortical flow from front to rear is observed inside the cell, which is believed to play an important role in this process (Bergert et al., 2015). The shapes of cells undergoing each mode of migration are also different. That is, cells performing amoeboid migration are relatively rounded, whereas those engaging in mesenchymal migration are relatively elongated (Haas and Gilmour, 2006). Recent studies, however, have begun to suggest that this concept of cell movement involving two distinct migration modes is too limited and does not allow the rigorous classification of all cell movements (Bodor et al., 2020). Indeed, some cells exhibit both mesenchymal and amoeboid-like movement modes and plastically switch between these, depending on the environmental conditions (Bergert et al., 2012; Ruprecht et al., 2015). Thus, some investigators have initiated studies aimed at identifying shared universal mechanisms underlying all cell migration.

From a mechanical modeling viewpoint, a number of common features present in both the mesenchymal and amoeboid modes of migration can be identified. For example, bleb formation in amoeboid migration and lamellipodia formation in mesenchymal migration are similar, given that, in both cases, the membrane in the front region of the cell tends to expand. Mechanically, this behavior of the cell membrane at the leading edge is expressed by weak surface tension. Strong attachment between membrane and substrate in mesenchymal migration and nonspecific friction in amoeboid migration are also expressed by one parameter of a mechanical model. That is, strong attachment is expressed by a large friction coefficient value between membrane and substrate, whereas weak nonspecific friction is expressed by a small friction coefficient value. Moreover, in both modes, contractions at the trailing end of the cell membrane are expressed by a strong surface tension in that region. These observations highlight the common mechanistic features underlying all forms of cell migration. Further, in both migration modes, cortical flow beneath the plasma membrane is present and is thought to play an important role in cell movement (Bray and White, 1988; Salbreux et al., 2012). However, as noted above, because there are many forces within cells, even if we focus only on the cell membrane, it is very hard to anticipate how cell membranes move and how cells ultimately move eventually under these myriad forces. Therefore, to better understand the mechanical mechanisms underlying cell migration, mechanical models that appropriately express forces within the cells and keep these forces balanced at each point on the cell membrane are needed.

A number of mechanical models for cell migration that satisfy these conditions have been developed. For example, some groups have proposed excellent three-dimensional (3D) surface models, in which directed surface flow and cell division are reproduced (Mietke et al., 2019; Bächer et al., 2021; Okuda et al., 2022). However, 3D mechanical models require a long computational time and are not appropriate for dealing with multiple cells simultaneously. In 2D cases, cellular vertex models are frequently used for describing multiple cell dynamics, wherein cells are approximated by polygons, and cell boundaries between adjacent cells are represented by straight segments (Fletcher et al., 2014). This model have succeeded in explaining important phenomena in epithelial sheets (Farhadifar et al., 2007; Rauzi et al., 2008; Aigouy et al., 2010; Fletcher et al., 2014; Sato et al., 2015a). However, if we extend this 2D cellular vertex model and try to more precisely describe cell surface dynamics on the substrate, some problems arise. One minor problem is that because the cell boundary between adjacent cells is represented by a straight segment, the model does not appropriately express the curvature of the cell boundary. This can be overcome relatively easily, however, by adding vertices to split the straight segment into multiple segments.

If we try to extend the 2D cellular vertex model to deal with curved cell boundaries with multiple segments, the expression of frictional force can be a major problem. In the current vertex model, only the vertices of polygons experience friction forces from the surrounding objects (Fletcher et al., 2014). This means that if a cell boundary is divided into some number of segments to express its curvature more smoothly, the friction forces on the cell boundary can change depending on the number of segments. For example, let us consider the case where we represent a straight boundary between cells A and B in two ways. One is that the cell boundary is represented by one segment specified by vertices 1 and 2. The other is that we add a new vertex 3 to the segment 12 and split the segment into two segments (i.e., the cell boundary is now represented by two segments, segment 13 and segment 32). Then, we consider the case where the cell boundary shifts slightly. In that motion, the latter representation of the cell

boundary obviously experiences a larger friction force than the former representation if the friction coefficients are the same, because the latter representation has three vertices whereas the former representation has two vertices. Friction force on the cell boundary should not depend on discretization of the cell boundary, but instead, should satisfy a continuous limit (i.e., the frictional force is expressed by a quantity per unit length of the cell boundary). Recently a 2D continuous mathematical model has been proposed that successfully reproduces the adhesion-independent movement of a single cell confined in a 3D space under axisymmetric conditions (Jankowiak et al., 2020). However, this model can assess only one cell. To comprehensively investigate cell migration, mechanical models capable of treating multiple cells that adhere to each other and satisfying force balance on the cell surface are necessary.

Here, we present a 2D cell membrane model, in which cells on a substrate are represented by polygons, and various forces on the cell surface, including contraction forces from actomyosin, adhesion between cells, and hydrostatic pressure from the cytosol, are implemented and balanced on the surface at all times. This model is equivalent to a continuous model if the lengths of segments representing the cell surface are kept within an appropriate range, using defined replacement rules, as described below. Cell clusters are represented by allowing a common surface between adjacent cells. We show that if cells in this model have a polarity expressed by direction-dependent surface tension, this causes the cell surface to flow from front to rear, and that flow induces unidirectional cell movement, not only for a single cell but also for a cluster of cells. In addition, if the surface-tension polarities of cells within the cluster are tilted with respect to the center of the cluster, the clusters rotate around the cluster center. This mechanical model produces movement while keeping forces balanced on the cell surface due to the inflow and outflow of cell surface components from inside the cell. The relationship between cell migration speed and turnover rate of cell surface components is discussed in Section 3.5.

2 Model

2.1 The situations treated by the mechanical model

We consider situations where cells are on a substrate; some cells exist individually on the substrate, while other cells are attached to each other to form a cluster. We focus on the dynamics of the peripheries of the cells, which movements are determined by force balance on the cell boundaries. Each cell has a polarity, and depending on the direction of the polarity, each cell changes the strength of contraction force on the cell boundary. We are concerned with two setups of cell polarity. One is that there is a chemoattractant gradient in a definite direction on the substrate, say the x-direction, and all cells have polarity in the x direction (Sections 3.2–3.6). The other is that cells that form a cluster have different directions of polarity. To be specific, the direction of polarity of each cell tilts with respect to the center of the cluster (Section 3.7). This tilted polarity may be achieved by chance or by using chirality of the cells (Taniguchi et al., 2011; Tee et al., 2015; Wan et al., 2016). A characteristic point of our model is that force balance holds at any parts of the cell boundaries at any time.

2.2 Setup of the model

In our model, cells on a substrate are represented by polygons; specifically, the α-th cell is represented by a polygon that consists of N_α segments and N_α nodes (Figure 1A). The number N_α can differ from cell to cell and changes with time, based on the following rules: if the segment under consideration becomes longer than some critical length ℓ^*_{long}, it is split into two segments by creating a new node at the center of the segment, and if the segment under consideration becomes shorter than some critical length ℓ^*_{short}, it is replaced by a single node whose position is the center of the segment before the replacement (Figure 1B). Using appropriate ℓ^*_{long} and ℓ^*_{short} values, the surface of the cell becomes smooth enough, and the dynamics of this discretized model are consistent with those observed in continuous models, as shown in Figures 1C, 2B, C. When a cell adheres to an adjacent cell, the segments and nodes on the cell boundary are shared between the two cells; that is, they have the same segments and nodes at their boundary (Figure 1A). Quantities assigned to the cell boundary, such as surface tension and rigidity of the cell boundary, are obtained by considering each quantity on the surfaces of the two cells, as in the existing vertex models (Fletcher et al., 2014).

Cell boundaries experience two types of forces: one is the frictional forces that are expressed by the dissipation function given in Eq. 1, and the other is the mechanical forces that are expressed by a potential function U in Eq. 2. Frictional forces arise from both external and internal factors. When the segments comprising the cells move with respect to the substrate, each segment bears a frictional force from the substrate, whose strength is proportional to the length and velocity of the segment. The frictional coefficient can depend on the direction of movement relative to the direction of the segment; that is, when the segment moves parallel to the direction of the segment, the frictional coefficient is $\eta_\parallel$, whereas when the segment moves perpendicular to the direction of the segment, the frictional coefficient is $\eta_\perp$. In addition, it is assumed that each segment has an internal friction; when a segment shrinks or expands, a resistance force arises within the segment. The strength of the internal friction is proportional to the strain rate of the segment, with the friction coefficient μ. Elongation or shrinkage of the segment is assumed to be an affine transformation (i.e., the segment is homogeneously elongated or shrunken). Under these assumptions, we can calculate the dissipation function W, which gives the frictional forces on segments in terms of only the positions and velocities of nodes on the cell surfaces (see Supplementary Appendix A for details), as

$$W = \sum_{\langle ij \rangle} \left\{ \frac{\eta_\parallel^{(ij)} \ell_{ij}}{2} \left(\left(\dot{X}_{ij} \cos\theta_{ij} + \dot{Y}_{ij} \sin\theta_{ij} \right)^2 + \frac{\left(\dot{\ell}_{ij} \right)^2}{12} \right) + \frac{\eta_\perp^{(ij)} \ell_{ij}}{2} \left[\left(\dot{X}_{ij}{}^2 + \dot{Y}_{ij}{}^2 + \frac{\left(\dot{\ell}_{ij} \right)^2}{12} + \frac{\left(\dot{\theta}_{ij} \ell_{ij} \right)^2}{12} \right) - \left(\left(\dot{X}_{ij} \cos\theta_{ij} + \dot{Y}_{ij} \sin\theta_{ij} \right)^2 + \frac{\left(\dot{\ell}_{ij} \right)^2}{12} \right) \right] + \frac{\mu^{(ij)}}{2} \frac{\left(\dot{\ell}_{ij} \right)^2}{\ell_{ij}} \right\}. \tag{1}$$

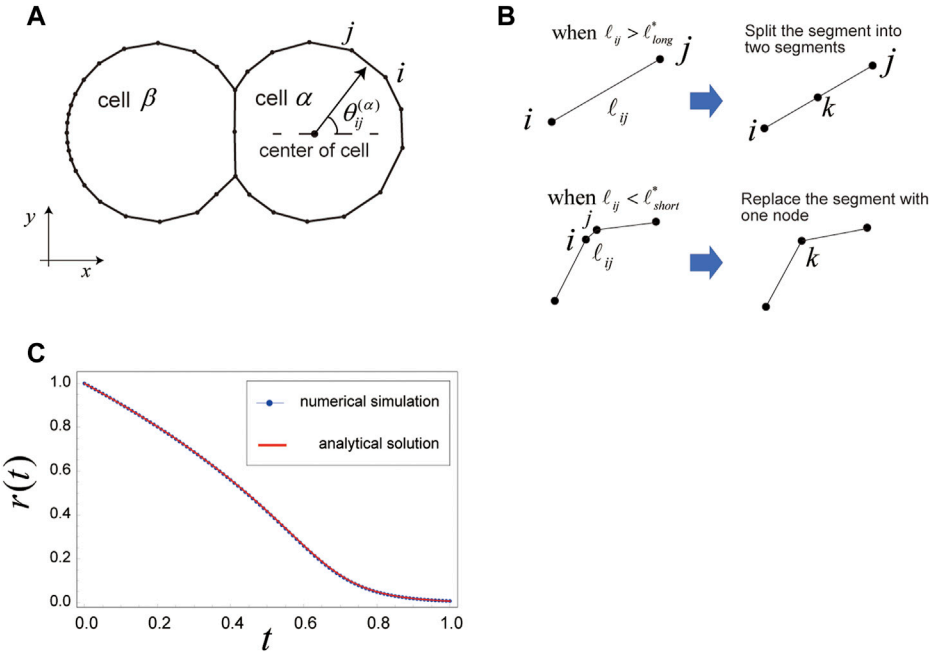

FIGURE 1
Setup for the two-dimensional (2D) cell membrane model of cell migration. **(A)** In this model, cells on a substrate are represented by polygons. If a cell adheres to an adjacent cell, the two cells share the segments and nodes on the joint boundary. The cell surface experiences various mechanical forces that are expressed by W and U in Eqs. 1, 2, respectively. These forces are balanced at all times on the cell surface, as shown in Eq. 3. **(B)** Replacement rules for cell boundary segments are as follows. When the length ℓ_{ij} of segment ij on a cell boundary exceeds a critical length, ℓ^*_{long}, the segment ij is split into two segments, ik and kj, at the next step, creating a new node k at the center of the previous segment ij. When ℓ_{ij} becomes less than a critical length, ℓ^*_{short}, the segment ij is replaced with a new node k, whose position is the center of the previous segment, ij. If appropriate lengths of ℓ^*_{long} and ℓ^*_{short} are chosen, the cell shape is kept smooth, and movement of the cell surface coincides with that observed under a continuous limit (e.g., Figures 2B, C). **(C)** Comparison between the numerical simulation and analytical solution for $r(t)$, where $r(t)$ is the radius of a circular cell that shrinks with constant surface tension $\gamma = 1$, and there are no constraints on area and perimeter of the cell. The parameters used here are as follows: $\eta = 1.0$, $\mu = 0.1$, $K = 0$, $K_p = 0$, $\kappa^{(ijk)} = 0$, and $\Delta t = 1/10000$. The initial configuration for the numerical simulation is a regular 40-sided polygon, with $r = 1$.

Here, ℓ_{ij} is the length of the segment that connects the ith and jth nodes; that is, $\ell_{ij} = |\mathbf{r}^{(i)} - \mathbf{r}^{(j)}|$, where $\mathbf{r}^{(i)} = (x_i, y_i)$ is the position of the ith node. $\mathbf{R}_{ij} = (X_{ij}, Y_{ij})$ is the position of the center of the segment ij, given by $\mathbf{R}_{ij} = (\mathbf{r}^{(i)} + \mathbf{r}^{(j)})/2$, and θ_{ij} is the angle between the x-axis and the vector from the i-th node to the j-th node. The dot over a quantity represents its time derivative, and the symbol $\langle ij \rangle$ under the summation symbol means that the sum is taken over all the segments in the system. Note that the sets of $\{\mathbf{R}_{ij}\}$, $\{\theta_{ij}\}$ and $\{\ell_{ij}\}$ are expressed by the set of positions of nodes, $\{\mathbf{r}^{(i)}\}$. Thus, as mentioned above, W is a function of $\{\mathbf{r}^{(i)}\}$ and $\{\dot{\mathbf{r}}^{(i)}\}$.

The frictional coefficients $\eta_{\parallel}^{(ij)}$, $\eta_{\perp}^{(ij)}$, and $\mu^{(ij)}$ in Eq. 1 can vary from segment to segment. However, our main objective is to show some simple applications of this model. We, therefore, kept these coefficients the same for every segment, such that $\eta_{\parallel}^{(ij)} = \eta_{\perp}^{(ij)} = \eta$ and $\mu^{(ij)} = \mu$ throughout this paper. Differentiating W in Eq. 1 with respect to the velocity the i-th node gives the frictional force $\mathbf{F}^{(i)}_{friction}$ on the i-th node as $\mathbf{F}^{(i)}_{friction} = -\partial W/\partial \dot{\mathbf{r}}^{(i)}$ (Landau and Lifshitz, 1976). Note that the dissipation function W in Eq. 1 considers the length dependence of the frictional force on the segment. Thus, even if a segment ij is divided into two segments, ik and kj, by adding a new node k, the total frictional forces on the segments ik and kj are the same as those on the segment ij before the division, provided movement of segments ik and kj is the same as that of segment ij. In this sense, the frictional force on the cell surface does not depend on the number of nodes on the cell surface and this model satisfies some continuous limits on the frictional forces.

The other mechanical forces on the cell surface, such as contraction forces coming from the actomyosin network beneath the plasma membrane and hydrostatic pressure from the cytosol, are represented by the following effective potential U, as follows:

$$U = \frac{K}{2}\sum_{\alpha}\left(A_\alpha - A_\alpha^{(0)}\right)^2 + \frac{K_p}{2}\sum_{\alpha}\left(L_\alpha - L_\alpha^{(0)}\right)^2 + \frac{1}{2}\sum_{\langle ijk\rangle}\kappa^{(ijk)}\left(\frac{\mathbf{r}^{(j)} - \mathbf{r}^{(i)}}{\ell_{ij}} - \frac{\mathbf{r}^{(k)} - \mathbf{r}^{(j)}}{\ell_{jk}}\right)^2 \frac{2}{\ell_{ij} + \ell_{jk}} + \sum_{\langle ij\rangle}\gamma_{ij}(t)\ell_{ij}, \tag{2}$$

where K, K_p, and $\kappa^{(ijk)}$ are non-negative constants. This form of U is quite similar to that given in existing vertex models (Farhadifar et al., 2007; Fletcher et al., 2014; Sato et al., 2015b), although it differs in the introduction of the third term, which represents the bending energy of cell membranes, and the form of $\gamma_{ij}(t)$, which expresses the strengh of surface tension on the cell membrane and is related to cell polarity.

The first term in Eq. 2 represents a pressure acting on the segments arising from the area difference between the current area of the cell, A_α, and its preferred constant value, $A_\alpha^{(0)}$. This

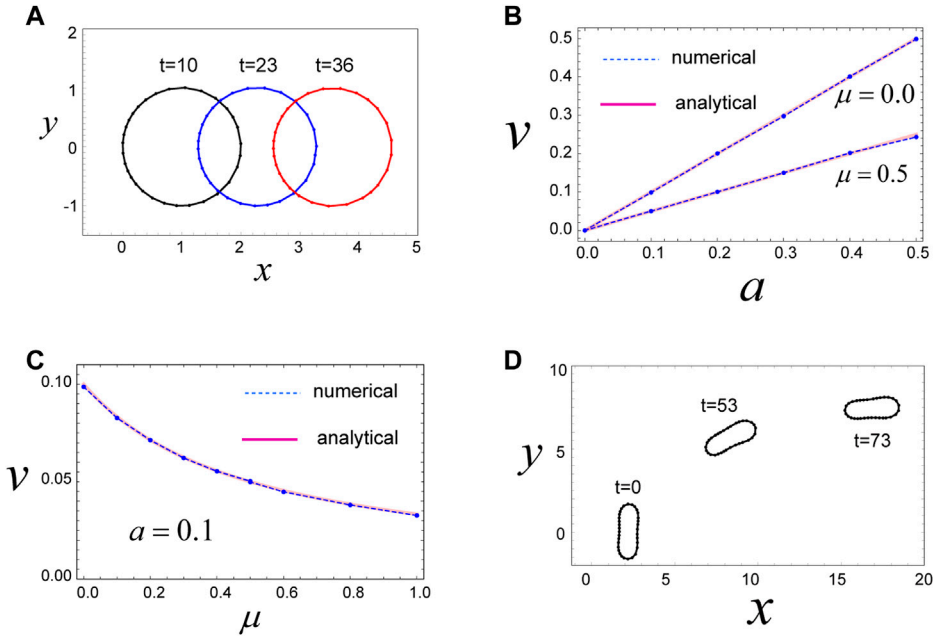

FIGURE 2
Mechanism for migration of a circular and non-circular cell. **(A)** A circular cell migrates in the x-direction due to the direction-dependent surface tension in Eq. 4, which generates a continuous flow of cell surface from front to rear. The cell movement is maintained as long as the cell has the polarity expressed by Eq. 4. Parameters used are as follows: $\mu = 0$, $\gamma_0 = 1.0$, $a = 0.1$, $\ell^*_{long} = 0.31$, $\ell^*_{short} = 0.12$, $K = 100$, $K_p = 0$, and $\kappa^{(ijk)} = 0$. **(B)** The steady speed v of circular cell movement as a function of a that represents the degree of polarization of the cell (see Eq. 4). The numerical results (dashed lines) and analytical results (red lines) show good agreement with one another, indicating that our discrete model, described by Eqs 1–3, coincides with a continuous model if we choose appropriate values for ℓ^*_{long} and ℓ^*_{short}. Parameters used are as follows: $\gamma_0 = 1.0$, $\ell^*_{long} = 0.31$, $\ell^*_{short} = 0.12$, $K = 100$, $K_p = 0$, and $\kappa^{(ijk)} = 0$. **(C)** The steady speed v of circular cell movement as a function of μ, which is the friction coefficient for internal friction of the cell surface, defined in Eq. 1. The analytical results (red curve) and numerical results (dashed curve) are in agreement with one another. Parameters used are as follows: $\gamma_0 = 1.0$, $a = 0.1$, $\ell^*_{long} = 0.31$, $\ell^*_{short} = 0.12$, $K = 100$, $K_p = 0$, and $\kappa^{(ijk)} = 0$. **(D)** A non-circular cell also migrates due to the direction-dependent surface tension in Eq. 4. In the final state, the long axis of the cell is aligned in the x-axis. Parameters used here are $\mu = 0$, $\gamma_0 = 0$, $a = 0.2$, $\ell^*_{long} = 0.4$, $\ell^*_{short} = 0.15$, $K = 1.0$, $K_p = 1.0$, $\kappa^{(ijk)} = 0.1$, and $L_0 = 0.25\,\pi$.

pressure can be interpreted as the hydrostatic pressure in the cytosol on the membrane of the cell. The α under the summation symbol indicates that the sum is taken over all cells in the system. The second term in Eq. 2 expresses the property that the cell tends to keep the perimeter length L_α at some preferable length $L_\alpha^{(0)}$. This term represents the tendency to conserve the amount of cell membrane (Fletcher et al., 2014; Sato, 2017). The third term in Eq. 2 expresses the bending energy of the membrane. The strength of the membrane against bending is characterized by the coefficient $\kappa^{(ijk)}$, such that, if $\kappa^{(ijk)}$ is large, the part of the membrane under consideration, expressed by segments ij and jk, is difficult to bend, and *vice versa*. The symbol $\langle ijk\rangle$ under the summation symbol indicates that the sum is taken over all pairs of segments that are connected and adjacent to each other. Lastly, the final term in Eq. 2 expresses the surface tension acting on the membrane, which is the result of both contraction forces from the actomyosin networks beneath the membrane and adhesion of the cell to outside objects, such as adjacent cells or substrate. Surface tension strength, expressed by γ_{ij}, is controlled by the cell via altered expression of proteins, such as myosin, actin, cadherin, and integrin. When contraction force is strong or adhesion is weak at segment ij, γ_{ij} becomes large, whereas when adhesion at segment ij is strong or contraction force is weak at segment ij, γ_{ij} becomes small.

Using this value of γ_{ij}, we can express the polarity of the cell. For example, consider the case where a cell has a polarity in the x-direction, and assume that the cell has a weak contraction force at the leading edge ($x > x_0$, where x_0 is the x-component of the position of the cell center) and a strong contraction force at the rear ($x < x_0$). This situation is expressed by letting the value of γ_{ij} depend on the relative position of the cell membrane with respect to the center of the cell. That is, a small value is assigned to γ_{ij} at the front of the cell, and a large value is assigned to γ_{km} at the rear. In this paper, we consider several cases with different assigned γ_{ij} values. If we accept the form of U given in Eq. 2, the total mechanical force $\mathbf{F}_U^{(i)}$ from U on the i-th node is given by $\mathbf{F}_U^{(i)} = -\partial U/\partial \mathbf{r}^{(i)}$.

In this model, we assume that the inertial force of the cell surface is negligible compared with the mechanical forces in question, and thus, all forces acting on the i-th node coming from U and W must be balanced at all times. That is,

$$-\frac{\partial W}{\partial \dot{\mathbf{r}}^{(i)}} - \frac{\partial U}{\partial \mathbf{r}^{(i)}}\bigg|_{\gamma_{jk}=\hat{\gamma}_{jk}} = 0 \tag{3}$$

holds for all i's at any given time. Here, the symbol $\gamma_{jk} = \hat{\gamma}_{jk}$ in the second term indicates that, after the derivative with respect to $\mathbf{r}^{(i)}$, each γ_{jk} in the second term is replaced by an explicit value $\hat{\gamma}_{jk}$, which is expressed as a function of $\{\mathbf{r}^{(i)}\}$ (Fletcher et al., 2014; Sato et al.,

2015b; Sato, 2017). This operation means that γ_{jk} obeys some other dynamics that are much faster than those of $\{\mathbf{r}^{(i)}\}$, such that γ_{jk} immediately reaches a value determined by $\{\mathbf{r}^{(i)}\}$ (Sato, 2017). If we accept that the dynamics of localization of molecules related to contraction, such as myosin, on the cell surface (tens of seconds) is much faster than that of cell membrane movement (a few minutes), this operation may be allowed. Eq. 3 gives the time evolution equations for $\{\mathbf{r}^{(i)}\}$.

2.3 Methods for numerical simulations

To numerically solve Eq. 3, we first nondimensionalize the variables and parameters appearing in the equation, using the following units: length, $\sqrt{A_0/\pi}$; time, $\eta/(K_0\sqrt{A_0/\pi})$; and energy, $K_0(A_0/\pi)^2$; where K_0 is a typical value of K solving for U in Eq. 2. Hereafter, we imply that the variables and parameters appearing in our model are nondimensionalized with the above units. For example, $A_0 = \pi$ and $\eta = 1$. We then numerically solve the nondimensionalized Eq. 3 for $\{\mathbf{r}^{(i)}\}$ by the Euler method, with the step size dt = 1/5000 or 1/10000. For each step, we further determine whether the length of each segment satisfies the replacement criteria $\ell^*_{long} < \ell_{ij}$ or $\ell^*_{short} > \ell_{ij}$. Any segments that satisfy either of these two conditions are replaced by the rules shown in Figure 1B.

3 Results

3.1 A case in which a circular cell isotropically shrinks with a constant surface tension

To test our model, we first determine whether the dissipation function W given in Eq. 1 appropriately expresses the frictional forces on the cell surface. For this we consider a case where a circular cell has a constant surface tension $\gamma = 1$ and no constraints on its area A and perimeter L; that is, we set $K = 0$, $K_p = 0$, and $\kappa^{(ijk)} = 0$ in Eq. 2. In this case, the circular cell shrinks with some speed, while maintaining its circular shape. The time series of the radius of the circular cell, $r(t)$, is analytically obtained (Supplementary Appendix B), resulting in $r(t) = \sqrt{\frac{\mu}{\eta} W_0\left(\frac{\eta}{\mu} e^{-\frac{2}{\mu}\left(\gamma_0 t - \left(\frac{\eta}{2} r_0^2 + \mu \log r_0\right)\right)}\right)}$, where $W_0(x)$ is the Lambert W function (the product logarithm) that satisfies $x = W_0(x)\, e^{W_0(x)}$ for $x > -1/e$. Comparing this analytical solution with the results of numerical simulation for Eq. 3 reveals good agreement (Figure 1C). Thus, we conclude that the friction force expressed by Eq. 1 appropriately expresses the frictional force experienced by the cell membrane, at least for this simple test case.

3.2 A circular cell migrates due to direction-dependent surface tension

Next, we investigate a more realistic case wherein the cell under consideration is circular with a constant area $A = A_0$ and has a polarity in the x-direction. Constant area of the cell is achieved by using the parameters $K \gg 1$, $K_p = 0$, and $\kappa^{(ijk)} = 0$ in Eq. 2, and cell polarity is expressed by the direction-dependent surface tension $\hat{\gamma}_{ij}$ in Eq. 3 as

$$\hat{\gamma}_{ij} = \gamma_0 - a\cos\theta^{(\alpha)}_{ij}, \tag{4}$$

where γ_0 is a positive constant, a is a non-negative constant, and $\theta^{(\alpha)}_{ij}$ is the angle between the x-axis and the vector connecting the center of cell α that contains segment ij and the center of segment ij (see Figure 1A). The value of a represents the degree of the polarity, such that, when $a = 0$, the cell is isotropic and has no polarity, whereas when $a > 0$, the cell boundary at a relatively large x has a weak surface tension, and the cell boundary at a relatively small x has a strong surface tension. Hereafter, we refer to the region of cell boundary at a relatively larger x as the "front" of the cell, and the region of the cell boundary at a relatively smaller x as the "rear" of the cell. If $a = 0$, the shape of the cell is circular due to the constant area and constant surface tension, γ_0, on the cell surface. In this simulation, we set a as a small positive value ($a \ll \gamma_0$), such that the circular shape of the cell is still retained.

We then examined the steady state of the cell with these model parameters. Numerical simulations reveal that the cell moves in the positive x-direction, with a constant speed, while keeping a circular shape in the steady state (Figure 2A). The driving force for this movement is the direction-dependent surface tension in Eq. 4 and the resulting cell surface flow from the front to the rear (Supplementary Movie S1). That is, in the front region of the cell, surface tension is relatively weak due to the parameters of Eq. 4, such that the surface in the front region tends to expand. In contrast, surface tension in the rear region of the cell is relatively strong, and hence, the surface in this region tends to shrink. This surface tension-dependent tendency of the cell surface to expand or shrink produces a flow of cell membrane, in which the front region is always expanding (in some sense, blebbing is continuously occurring in front of the cell), whereas the rear region is always shrinking (Supplementary Movie S1). These behaviors act as a source and sink of cell surface and yield a flow of cell surface from front to rear. In addition, within this system, there is a frictional force between the cell surface and the substrate. Thus, if the cell surface moves in some direction, the whole cell experiences forces that move it in the opposite direction, based on the action–reaction principle.

The velocity $\mathbf{V}$ of this cell movement resulting from the direction-dependent surface tension can be analytically calculated, by treating the cell as a continuous circular object (see Supplementary Appendix C for details). The result ist

$$\mathbf{V} = \left(a/\left(\eta R\left(1 + 2\mu/\left(\eta R^2\right)\right)\right), 0\right), \tag{5}$$

where R is the radius of the circular cell. We then compared this analytical solution with the cell speed obtained by numerically solving Eq. 3 and found that these values are in good agreement with each other (Figures 2B, C). This indicates that our discrete model described by Eqs. 1–3 can describe continuous cell surface dynamics if we choose appropriate values for parameters, such as ℓ^*_{long} and ℓ^*_{short}.

3.3 An elongated cell migrates due to direction-dependent surface tension

We further find that single-cell migration induced by direction-dependent surface tension, described in Eq. 4, occurs even when the cell shape is elliptical (Figure 2D). We

can model an elliptical-shaped cell using finite values for K_p and $\kappa^{(ijk)}$ in Eq. 2 and by ensuring the preferred cell perimeter L_0 is longer than that of a circle with the area A_0, $2\sqrt{\pi A_0}$. Overall, the mechanism for cell movement is basically the same as for circular cells, that is, the surface flows from front to rear due to direction-dependent surface tension, described in Eq. 4. In this simulation, we set the initial configuration of the cell, such that the long axis is aligned in the y-direction (Figure 2D; $t = 0$). Initially, up until $t = 8$, the elliptical cell moves in the x-direction, while keeping the short axis of the cell aligned with the x-axis. However, at around $t = 25$, the long body axis begins to incline toward the x-direction, and the direction of cell movement also begins to incline; that is, the cell has the y-component of velocity (Supplementary Movie S2). In the final stage, the long body axis is completely oriented to the x-axis, and the cell moves in the x-axis again. The final speed of the cell is faster than in the earlier stage, where the long axis of the cell is perpendicular to the x-axis. This simulation indicates that if the cell shape is elliptical and the direction of cell polarity is fixed in the x-axis, cell movement in which the short axis is oriented to the x-axis is slow and unstable, whereas cell movement in which the long body axis is oriented to the x-axis is fast and stable. In general, the parameters of Eq. 4 make cell movement fast if the long axis of the cell is directed in the direction of cell polarity. This property clearly appears in the next case, where the cell is sandwiched by two parallel walls.

3.4 A case in which a cell is sandwiched by two walls

Motivated by results from published experiments (Bergert et al., 2015; Liu et al., 2015; Sakamoto et al., 2022), we next examined the scenario in which a cell is sandwiched by two parallel walls. In this case, the wall is expressed using the potential $U_{wall}(y) = (y - d)\Theta(y - d) - (y + d)\Theta(-y - d)$, where d is one-half the distance between the walls, and $\Theta(x)$ is the Heaviside step function, defined as $\Theta(x) = 1$, for $x > 0$, and $\Theta(x) = 0$, for $x \leq 0$. By adding the terms $\sum_{all\ nodes\ i's} U_{wall}(y^{(i)})$ to Eq. 2, the cell surface close to the walls experiences a repulsive force from the wall potential. In this setup, the area of the cell is held constant as $A = A_0$, which is achieved with the same parameters as used for the simulation with a circular cell. Under these conditions, the cell also migrates in the x-direction in the steady state (Figure 3A), where the speed of the cell increases as d decreases (Figure 3B), consistent with published experimental results (Liu et al., 2015; Sakamoto et al., 2022). To demonstrate how and why cell speed increases with decreased d, we derive the analytical expression for the speed of the cell (see Supplementary Appendix C), which is given by

$$V_x = \frac{2}{\pi\eta d}\left(\int_0^{\pi/2} \sin\xi_1 \frac{d\gamma(\theta_{forward}(\xi_1))}{d\xi_1}\, d\xi_1 + \int_{\pi/2}^{\pi} \sin\xi_2 \frac{d\gamma(\theta_{backword}(\xi_2))}{d\xi_2}\, d\xi_2\right) + \frac{2\Delta\gamma}{\pi\eta d}, \tag{6}$$

where $\theta_{forward}(\xi_1) = \arctan\left(\frac{d\sin\xi_1}{d\cos\xi_1 + L_x}\right)$, $\theta_{backword}(\xi_2) = \arctan\left(\frac{d\sin\xi_2}{d\cos\xi_2 - L_x}\right)$, and $\Delta\gamma = \gamma(\pi - \theta_1) - \gamma(\theta_1) = 2aL_x/\sqrt{{L_x}^2 + d^2}$. The

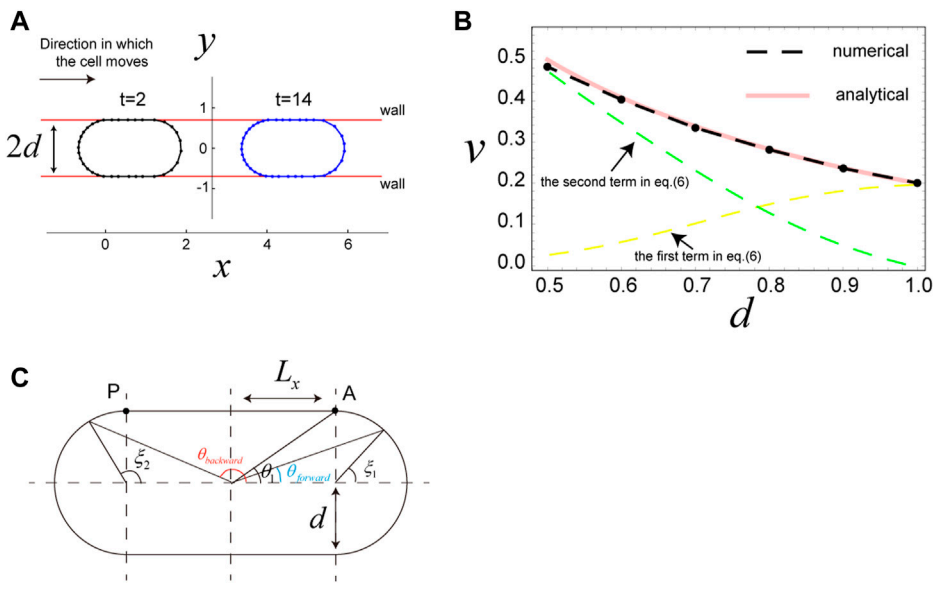

FIGURE 3
Migration of a cell sandwiched by two walls. **(A)** Snapshots of a cell sandwiched by two walls, which migrates in the x-direction due to surface flow resulting from the direction-dependent surface tension in Eq. 4. The distance between the two walls is $2d$; a decrease in d increases migration speed, v, of the cell (see panel B). Parameters used are as follows: $d = 0.7$, $\mu = 0$, $\gamma_0 = 1.0$, $a = 0.2$, $\ell^*_{long} = 0.31$, $\ell^*_{short} = 0.12$, $K = 100$, $K_p = 0$, and $\kappa^{(ijk)} = 0$. **(B)** The steady speed, v, of a cell sandwiched by walls as a function of d. The dashed black curve shows the numerical results, and the red curve represents the analytical results from Eq. 6, which are in good agreement. The yellow and green dashed curves are the first and second terms in Eq. 6, respectively. Parameters used here are the same as in panel A, except that d is varied. **(C)** Geometrical explanation of the quantities θ_1, $\theta_{forward}$, $\theta_{backword}$, ξ_1, and ξ_2 in Eq. 6.

angles $\theta_{forward}$, $\theta_{backward}$, ξ_1, and ξ_2 used here are defined as shown in Figure 3C. The values L_x and d are the half-length of the straight part of the cell and the radius of the circular part of the cell, respectively. Because the total area of the cell is kept at $A = A_0$, L_x and d are related as $4L_x d + \pi d^2 = A_0$.

Results from analytical expression Eq. 6 are in good agreement with the results of numerical simulations (Figure 3B). Thus, we use Eq. 6 to interpret the cell speed in this scenario. The first term in Eq. 6 is the contribution from surface flow on the two semicircles of the cell, and the second term is the contribution from surface flow on the straight parts of the cell. When d becomes small, the semicircles also become small, and the flow speed of cell surface along the semicircles becomes slow due to the surface tension gradient along the small semicircles. Thus, the first term in Eq. 6 becomes small when d decreases (Figure 3B, yellow dashed curve). In contrast, $\Delta\gamma$ in the second term in Eq. 6, which is the surface tension difference between the two edges of the straight parts of the cell (Figure 3C), increases with decreased d (see Eq. 4). Furthermore, d in the denominator of the second term in Eq. 6, which represents the resistance of the semicircle parts to the cell movement, also enlarges this term as the value of d decreases. Thus, the whole second term in Eq. 6 drastically increases when d decreases (Figure 3B, green dashed curve). The tendency that the migration speed v of the sandwiched cell increases with decrease in d appears even when we take a different setup of $\hat{\gamma}_{ij}$. For example, we consider the case where the surface tension is constantly increased along the cell surface form front to rear, in which the minimum and maximum surface tensions are kept to be constant, i.e., $\hat{\gamma}_{ij} = 0.8$ at the front and $\hat{\gamma}_{ij} = 1.2$ at the rear. These values are the same as those in the simulations in Figure 3B. The results of numerical simulations with this setup is given in Supplementary Figure S2, where as in Figure 3B v increases with decrease in d, while the d dependence of v is somewhat moderate compared to Figure 3B. This same tendency of v implies that the increase in v of the sandwiched cell with decrease in d may be a robust phenomena, as frequently observed in experiments (Bergert et al., 2015; Sakamoto et al., 2022).

3.5 Properties of surface flow-mediated cell migration

To better understand why and how cells move due to surface flow while keeping the forces balanced at all times, we surveyed the properties of cell movement observed in this model. Although these properties derived below are provided in a continuous form, it is not difficult to translate them into a discrete form. As noted above, our model neglects all inertia of the cell surface, so that the forces on any element of the cell surface are balanced at any time, and more importantly, the total force on the cell surface from the substrate must vanish at any time. Because the force on the cell surface from the external object—the substrate—is friction only, we have the following equality:

$$\int_\Omega \eta \mathbf{v}(\xi,t)\frac{\partial s(\xi,t)}{\partial \xi}d\xi = 0, \tag{7}$$

at any time t. Here, ξ is the material coordinate that is assigned to the element of cell surface under consideration and $s(\xi,t)$ is the counter length of the arc of cell surface between some reference point on the cell surface and the cell surface element specified by ξ at time t. Additionally, $\mathbf{v}(\xi,t)$ is the velocity of the surface element at ξ and t; Ω under the integral symbol indicates that the range of the integral is the whole cell surface. We then consider the situation where cell movement reaches a steady state, with cell velocity and cell shape constant in time, focusing on some time t_0 in this steady state. At $t = t_0$, we reassign the material coordinate ξ on the cell surface, such that ξ coincides with the counter length s; that is,

$$s(\xi,t_0) = \xi. \tag{8}$$

With this situation, let us consider the time evolution of the cell surface density, ρ. In general, ρ obeys the following time evolution equation

$$\partial\rho(\xi,t)/\partial t = -\left((\partial\mathbf{r}/\partial\xi)\cdot(\partial\mathbf{v}/\partial\xi)\right)/\left(\partial s/\partial\xi\right)^2\rho + J(\xi,t), \tag{9}$$

Where $\mathbf{r}(\xi,t)$ is the position vector of the surface element at ξ and t, and J is the flux of cell surface component from the cell inside to the cell surface per unit length. The derivation of Eq. 9 is shown in Supplementary Appendix D. In the steady state, ρ is constant in time, say $\rho = \rho_0$, and the time derivative $\partial\rho/\partial t$ is zero. Thus, from Eqs. 8, 9 we obtain

$$J(\xi,t_0) = \rho_0\,(\partial\mathbf{r}/\partial\xi)\cdot(\partial\mathbf{v}/\partial\xi), \tag{9.1}$$

which describes the relationship between J, $\mathbf{r}$, and $\mathbf{v}$ in the steady state. Because of the constant cell shape in the steady state, the total flux of the cell surface components must vanish at any time. Thus,

$$\int_\Omega J(\xi,t_0)d\xi = 0. \tag{10}$$

Interestingly, J in Eq. 9.1 is related to the cell migration velocity $\mathbf{V}$ in the steady state for the following reasons. In the steady state, the cell surface center of mass also moves with the same velocity $\mathbf{V}$. However, as indicated in Eqs. 7, 8, there is no net velocity of components on the cell surface, i.e., $\int_\Omega \mathbf{v}(\xi,t_0)d\xi = 0$. This implies that the shift in cell surface center of mass is, in fact, achieved by the inflow and outflow of cell surface components from inside the cell. Thus, the integral of the product of $J(\xi,t_0)$ and $\mathbf{r}(\xi,t_0)$ over the whole cell surface gives the transport rate of cell surface components through the inside of the cell. Dividing this quantity by the total amount of components on the cell surface, $\rho_0 L_{cell}$, yields the velocity of the cell surface center of mass. Therefore,

$$\mathbf{V} = \int_\Omega \mathbf{r}(\xi,t_0)J(\xi,t_0)d\xi/\rho_0 L_{cell}, \tag{11}$$

where L_{cell} is the cell perimeter in the steady state. Eq. 11 is interesting because this relation connects apparently different quantities, the cell migration velocity $\mathbf{V}$ and the turnover rate J of the cell surface. Indeed, we can confirm that Eqs. 7, 10, and 11 exactly hold for the circular cell migration case with $\mu = 0$ as shown below. From the analytical results given in Equation (C.16) in Supplementary Appendix C, $\mathbf{r}$ and $\mathbf{v}$ of the circular cell in the steady state are given as

$$\begin{aligned}\mathbf{r}(\xi) &= \left(\frac{a}{\eta R}t + R\cos\frac{\xi}{R}, R\sin\frac{\xi}{R}\right)\\ \mathbf{v}(\xi) &= \left(\frac{a}{\eta R} - \frac{2a}{\eta R}\left(\sin\frac{\xi}{R}\right)^2, \frac{2a}{\eta R}\sin\frac{\xi}{R}\cos\frac{\xi}{R}\right)\end{aligned}. \tag{12}$$

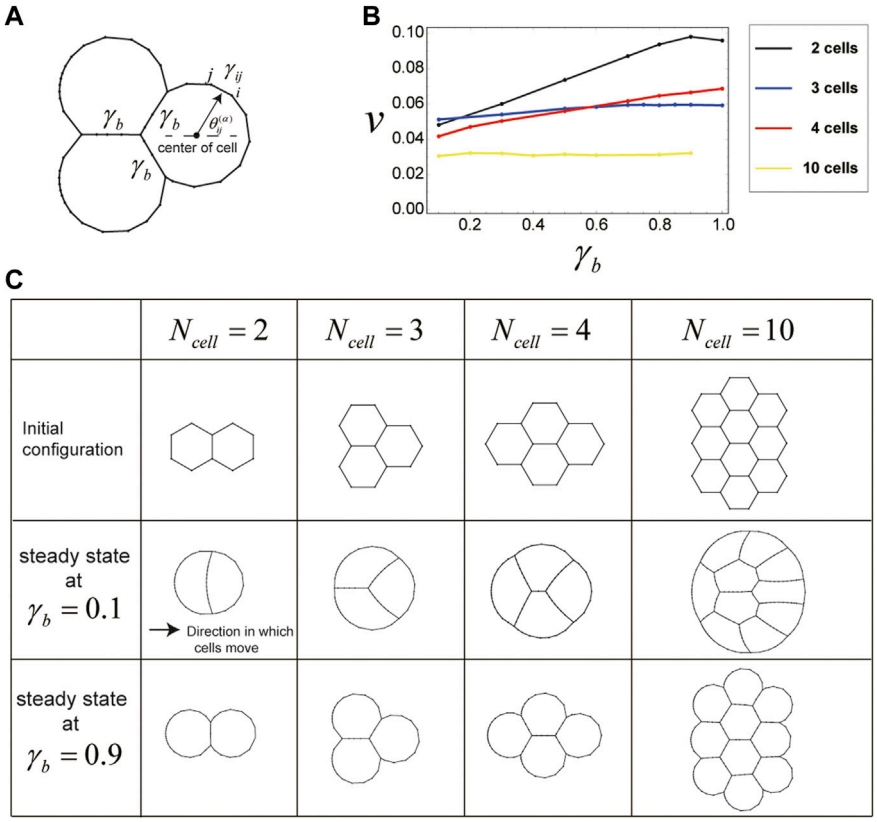

FIGURE 4
Cells in a cluster also migrate due to direction-dependent surface tension. **(A)** Setup for the surface tension of cells in a cluster. The boundaries between any two cells in the cluster have a constant surface tension γ_b, whereas the other cell surfaces, which are outside of the cluster, have the direction-dependent surface tension expressed by Eq. 4. **(B)** The steady speed v of cell cluster migration as a function of γ_b, for each cell number N_{cell}. When γ_b is increased, cluster migration speed also tends to increase. Parameters used here are as follows: $\mu = 0$, $\gamma_0 = 1.0$, $a = 0.1$, $\ell^*_{long} = 0.6$, $\ell^*_{short} = 0.08$, $K = 100$, $K_p = 0$, and $\kappa^{(ijk)} = 0$. **(C)** Shapes of cells in the cluster during steady state migration for each N_{cell} and γ_b.

From Eqs 9.1–12, we have

$$J = \rho_0 \frac{2a}{\eta R^2} \cos \frac{\xi}{R}. \tag{12.1}$$

Inserting Eqs. 12–12.1 into Eq 11 gives

$$\mathbf{V} = \left(\frac{a}{\eta R}, 0 \right), \tag{12.2}$$

where we have used $L_{cell} = 2\pi R$ and the fact that the range of ξ is $[0, 2\pi R]$. Eq. 12.2 coincides with Eq. 5 for the case of $\mu = 0$.

3.6 Multiple cells in a cluster also move via direction-dependent surface tension

The above simulations focus on migration of individual cells; however, cells often move together with other cells. Therefore, we next examined whether cell migration due to direction-dependent surface tension occurs even when multiple cells are attached to each other, forming a cluster. Specifically, we investigated the case where the number N_{cell} of cells on the substrate is $N_{cell} = 2, 3, 4, 10$ with some initial configuration in which the cells are attached to each other (Figure 4C). In these simulations, we have set the surface tension on the boundary between the cells to a constant value (*i.e.*, $\gamma = \gamma_b$), by assuming that the same type of cells is adhering to each other with some characteristic strength (Figure 4A). The other cell boundaries, which do not contact other cells, have the direction-dependent surface tension specified by Eq. 4. As in the case of single-cell migration investigated in Sections 3.2–3.4, each cell in this system keeps its area constant and has no constraint on its perimeter; that is, $K = 100$, $K_p = 0$, and $\kappa^{(ijk)} = 0$ in Eq. 2. Under these conditions, multiple cells move in the x-direction, while maintaining attachment between cells in the steady state (Figure 4C, Supplementary Movies S3–S10). Moreover, the mechanism of multiple-cell migration is basically the same as that of single-cell migration. That is, due to the direction-dependent surface tension of each cell, the surface of the cell cluster flows from front to rear, and this flow drives movement of the whole cluster.

The shape and velocity of the cluster during this movement depend on the value of γ_b. When γ_b decreases, the shape becomes round, and speed becomes slow (Figures 4B, C). The roundness of the cell cluster at small γ_b results from the constant area and lack of constraint on the perimeter of each

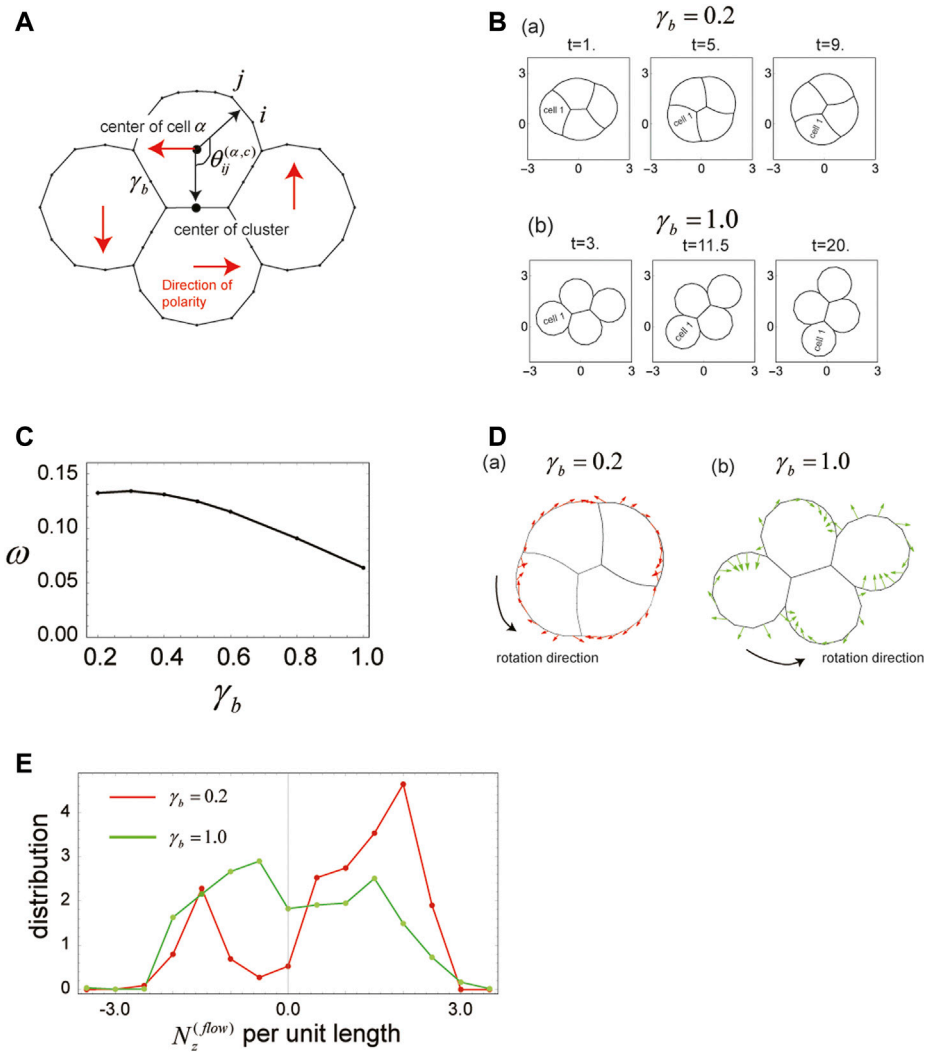

FIGURE 5
Cells in a cluster rotate when the polarity of each cell is tilted with respect to the cluster center. **(A)** Geometrical explanation of the angle $\theta_{ij}^{(a,c)}$ used in Eq. 13. Polarity of each cell in the cluster is indicated by the red arrow, which has a direction perpendicular to the vector from the cell center to the center of the cluster. **(B)** Snapshots of the cell cluster, rotating counterclockwise about the center of the cluster due to the direction-dependent surface tension in Eq. 13. Parameters used are as follows: $\mu = 0$, $\gamma_0 = 1.0$, $a = 0.1$, $\ell^*_{long} = 0.6$, $\ell^*_{short} = 0.08$, $K = 100$, $K_p = 0$, and $\kappa^{(ijk)} = 0$. In **B(a)**, $\gamma_b = 0.2$ and in **B(b)**, $\gamma_b = 1.0$. **(C)** The angular velocity, ω, of cluster rotation as a function of γ_b. **(D)** Velocities of the cell surface during rotation. **(a)** Red arrows indicate the cell surface velocities for $\gamma_b = 0.2$. **(b)** Green arrows indicate the cell surface velocities for $\gamma_b = 1.0$. The velocities for $\gamma_b = 0.2$ are oriented closer to the tangent of the cell surface, compared with those for $\gamma_b = 1.0$. **(E)** Distribution of the z-component of the torque generated by surface flow, which is induced by the direction-dependent surface tension in Eq. 13. When $\gamma_b = 0.2$, stronger torques that rotate the cluster more rapidly are generated, compared with the torques produced when $\gamma_b = 1.0$.

cell. Due to these parameters, when γ_b becomes small, boundaries between cells tend to extend, and the whole cell cluster behaves like one object. Further, because the cell cluster surface has a constant surface tension, γ_0, from Eq. 4, which reduces the cluster perimeter as much as possible under the constant area, $A_{cluster} = N_{cell}A_0$, the whole cluster is nearly a circle. In contrast, when γ_b becomes large, boundaries between cells tend to shrink, and outer cells within the cluster tend to be round, with the surface tension γ_0 (Figure 4C).

The slow cluster movement speed at small γ_b results from the roundness of the cell cluster. As shown in Sections 3.2–3.4, surface flow-induced cell migration, in general, becomes fast when the cell is elongated in the x-axis. This tendency is most evident in the case of a cell sandwiched by two walls, described in Section 3.4, where $\Delta\gamma$ in Eq. 6 acts as the driving force for movement. Similarly, in the case of cluster migration, the surface tension gradient along the cell surface (and the resultant flow of cell surface) is also the driving force for movement. Thus, if cells within the cluster are relatively elongated in the x-direction, the speed of cluster movement is relatively fast. However, when the cluster is round, such as for $N_{cell} = 2, 4$ and $\gamma_b = 0.1$ (Figure 4C), each cell in the cluster is relatively elongated in the y-axis, and thus, the driving forces are small, and the movement becomes slow.

3.7 Cell clusters rotate when cell direction is tilted with respect to the center of a cluster

To this point, we have examined only scenarios in which all cells on a substrate have the same direction of polarity (e.g., the x-direction). However, because clustered cells may also show distinct polarities, we next investigated the case wherein direction of polarity for individual cells within a cluster differs from cell to cell. In particular, we considered four cells comprising a cluster, in which each individual cell has a polarity that is directed perpendicular to the direction from the center of the cell to that of the cell cluster (Figure 5A). Surface tension for cells within this situation is expressed as

$$\hat{\gamma}_{ij} = \gamma_0 - a\cos\left(\theta_{ij}^{(\alpha,c)} - 3\pi/2\right), \tag{13}$$

where $\theta_{ij}^{(\alpha,c)}$ is the angle between the vector from the center of cell α that contains segment ij to the center of the cluster and the vector from the center of cell α to the center of segment ij (Figure 5A). The other parameters for this simulation are the same as those for cluster migration investigated in Section 3.6; that is, boundaries between cells within the cluster have a constant surface tension, $\gamma_{ij} = \gamma_b$, and each cell in the cluster keeps its area constant and has no constraint on its perimeter, with $K = 100$, $K_p = 0$, and $\kappa^{(ijk)} = 0$ in Eq. 2.

The initial configuration of the cell cluster is the same as in Figure 4C ($N_{cell} = 4$). Numerical simulations with the above parameters further indicate that each cell within the cluster continues to rotate counterclockwise around the center of the cluster while maintaining its attachments (Figure 5B; Supplementary Movies S11, S12). This rotation continues as long as each cell has the polarity established in Eq. 13, and the mechanism of movement is basically the same as observed for cluster migration and single-cell migration. That is, cells move due to the direction-dependent surface tension expressed by Eq. 13; the surface of the cell cluster moves clockwise, and this surface movement generates the driving force for rotational movement of the whole cluster. In this simulation, we set the polarities of the cells in the cluster with Eq. 13. However, in reality it may be more reasonable that the direction of cell polarity changes with time by following some other rules. One such rule is called the velocity alignment mechanism (Camley et al., 2014), in which cells align their polarity to their velocity. We incorporated this rule into our model and performed numerical simulations. The results show that for any initial directions of cell polarity, the cell polarities finally align such that the cluster of cells rotates (Supplementary Movies S13, S14). The direction of rotation depends on the initial distribution of cell polarities in the cluster. That is, the cell cluster rotates clockwise or counter clockwise depending on the initial distribution of cell polarities. Our system does not require cell confinement for this rotational motion, which is different from the results of previous studies (Camley et al., 2014).

As in the case of single-polarity cluster migration examined in Section 3.6, shape and rotational velocity of the cell cluster change with γ_b (Figures 5B, C). When γ_b is small, the cell cluster becomes round, and the angular velocity for the rotational movement of the cluster becomes large. The reasons for this cluster roundness are the same as those outlined in Section 3.6, that is, the whole cluster behaves like one object due to a lack of constraint on cell perimeter and small γ_b. In addition, the constant surface tension, γ_0, reduces cluster surface as much as possible under the constant whole area, $A_{cluster} = N_{cell}A_0$.

The faster rotation of the cell cluster at small γ_b originates from the velocity distribution of the cell cluster surface (Figure 5Da), and the reasons for this are as follows. First, cell boundaries within the cluster are classified into one of two types: 1) Cell boundaries that are located at the surface of the cluster and are associated with only one cell, referred to as the "outer cell boundaries" and 2) cell boundaries that are located within the cluster and form boundaries between two adjacent cells, referred to as "inner cell boundaries." During rotation of the cluster, the driving forces for cluster movement come from the flow of the outer cell boundaries, because only the outer cell boundaries have cell polarity, as indicated by Eq. 13. In the case of the round cluster ($\gamma_b = 0.2$; Figure 5Da), most velocities of the outer cell boundaries are directed in the tangent of the cluster surface, which comes from the monotonic decrease in surface tension along the surface. These velocities generate a large magnitude of torque compared with those present in the case of $\gamma_b = 1.0$ (see Figures 5D, E). Here, $N_z^{(flow)}$ is the z-component of the torque generated by the surface flow of the outer cell boundaries and is evaluated as $N_z^{(flow)} = -\eta\sum_{\langle ij\rangle_{outer}}((\mathbf{R}_{ij} - \mathbf{r}_c) \times (\dot{\mathbf{R}}_{ij} - \dot{\mathbf{r}}_c))_z \ell_{ij}$, where $\mathbf{r}_c$ is the position vector of the cluster center, and $\langle ij\rangle_{outer}$ indicates that the summation range is over all outer cell boundaries. $N_z^{(flow)}$ is balanced with the z-component of torque generated from frictional forces experienced by the inner cell boundaries, denoted by $N_z^{(friction)}$, and this balance determines the angular velocity, ω, of the cluster rotation. $N_z^{(friction)}$ is roughly expressed as $N_z^{(friction)} = -\zeta\omega$, where ζ is a coefficient given by $\zeta = \eta\sum_{\langle ij\rangle_{inner}}|\mathbf{R}_{ij} - \mathbf{r}_c|^2\ell_{ij}$. The ζ coefficient is almost constant in time because it is determined by the shape of the network of inner cell boundaries, which is also almost constant in time (see Supplementary Movies S11, S12). The torque balance on the cell surface gives $\omega = N_z^{(flow)}/\zeta$. Although both $N_z^{(flow)}$ and ζ increase with decreased γ_b (Supplementary Figure S1), the increase in ζ is more gentle than for $N_z^{(flow)}$, which results from the fact that the size of the network of inner cell boundaries does not change much with γ_b (see Figure 5B). Thus, the increase in $N_z^{(flow)}$, which occurs with decreased γ_b, increases the angular velocity ω.

4 Discussion

In this study, we have developed a 2D cell membrane model, described by Eqs 1–3, which shows that cells on a substrate migrate due to direction-dependent surface tension, represented by Eq. 4. Notably, this is true, not only for a single cell but also for multiple cells that adhere to one another and form a cluster. Moreover, if we change the direction of cell polarity within a cell cluster, such that polarity varies from cell to cell, as in Eq. 13, the cell cluster rotates due to direction-dependent surface tension. A key point of emphasis is that, because this model neglects any inertia of the cell surface and ensures that forces are balanced on the cell surface at all times, the total force exerted on each cell from outside objects, such as the substrate and neighboring cells, always vanishes. That is, the cell movement in this situation is, what we call, "force free", and this is driven by the inflow and outflow of cell membrane components from inside the cell, as discussed in Section 3.5.

Although this is a 2D model, it is expected that the cell movement we observe herein, namely, single-cell migration, cluster migration, and cluster rotation, may also be present in 3D models, because the mechanism of movement (i.e., direction-dependent surface tension) is likely applicable to 3D cases. Indeed, single-cell migration due to direction-dependent surface tension has been demonstrated in a previously published study (Okuda et al., 2022), for a spherical cell migrating with a constant velocity in 3D space. Thus, we anticipate that cluster migration and rotation will be shown in well-implemented 3D models.

We further expect this model may reveal relevant information for better understanding cell shape and cortical flow during cell movement in real-life situations. This is because, as previously emphasized, our model satisfies force balance on the cell membrane at all times, and hence, the cell shapes appearing in this model are the results of that force balance on cell surface during cell migration (e.g., see Figures 2D, 4C). Thus, if a parameter set in our model mimics the cell shapes and cell movement observed in experiments, we can expect which part of the cell experiences strong contractile forces and which part of the cell membrane has strong stiffness by looking at the experimental results. In addition, this mechanical model provides the speed of cell movement. Thus, with these properties we can address the relationship between cell shape and cell velocity, which is proposed in the existing works (Ohta and Ohkuma, 2009) by using a symmetry argument. We can examine the relationship between shape and speed of cells by the cell-level model. In addition, by regarding the segments in our model as the cortex in cells, we are able to investigate cortical flow within moving cells, as in previously published studies (Jankowiak et al., 2020). A key point of the present model is that due to the discreteness of this model, we can easily set the parameter values that specify key characteristics of the cells we are modeling. For example, we can change the strength of contractile and frictional forces, as well as the stiffness of the cortex, by changing γ_{ij}, η_{ij}, and $\kappa^{(ijk)}$ in space and time. For example, cells change its behaviors depending on the stiffness of the substrate (Durotaxis) (Lo et al., 2000). By setting up that the values of γ_{ij}, η_{ij}, and $\kappa^{(ijk)}$ depend on the stiffness of the substrate in some way in our model, we can investigate effects of the stiffness of the substrate on the cell movement from a subcellular level.

In our model, as already mentioned in Section 2.1, we focused on the dynamics of the cell peripheries. However, in many real-life cases, cells are attached to the substrate at some focal adhesions, and the two-dimensional flow of the cortex at the bottom region of the cells is also important for cell movement. Therefore, it would be a good strategy to extend the presented cortex model to a model that expresses the two-dimensional flow on the plane. This will be a target of future work. In addition, it has been observed that the plasma membrane and the cortex beneath the plasma membrane move separately during cell movement (Taniguchi et al., 2023). This observation implies that it is more realistic for a model of cell movement to describe the dynamics of two components, the plasma membrane and the cortex. This will also be a target of future research.

In the current remodeling rules for segments that represent cell boundaries, given in Section 2.2, the attachment and detachment of cells, which are important processes for considering more general movement of cells, are not described. In fact, by adding only some rules to the current setup, we can describe the attachment and detachment of cells. An example of it is as follows. When two separated cells are close to each other and the distance between some parts of two cell surfaces becomes shorter than some critical distance, then the parts of cell surfaces are merged and becomes one segment. This setup describes the attachment of two cells. In addition, when the common cell boundary between two adhered cells becomes shorter than some critical length, then the common cell boundary is split into two cell boundaries and two cell are separated. This situation represents the detachment of two cells. By introducing this rule into the current version, we can investigate more complex behaviors of cells on a substrate.

In the present paper, we have assumed that cell polarity is represented by the direction dependence of γ_{ij}. However, because the front and rear of a cell differ in regard to the stiffness of the cell surface and the strength of attachment to the substrate, it may be more plausible to model the situation in which cell polarity can change the cell stiffness, $\kappa^{(ijk)}$, as well as the friction coefficients, η_{ij} and μ_{ij}. By doing so, we may reproduce more realistic cell behaviors, such as blebbing (Paluch and Raz, 2013). We can also consider many variations of the form of $\hat{\gamma}_{ij}$. For example, since the position of nucleus in a cell plays an important role for cell dynamics (Moure and Gomez, 2020), it may be more realistic thet the value of $\hat{\gamma}_{ij}$ is determined by the relative position of the cortex to the nucleus.

In the present paper cell polarity was *a priori* given as in Eqs. 4, 13. But in reality, the direction of cell polarity dynamically changes with time depending on the environment surrounding the cell and the state of itself. Many possible ways for describing the time evolution of cell polarity have been proposed (Camley et al., 2014). By introducing proposed descriptions of cell polarity into our mechanical model and comparing the results obtained by the model to experiments, we might be able to determine which time evolution rule for cell polarity is most appropriate.

The phenomenon of cells migrating on a substrate, while forming a cluster, has been observed during development of the zebrafish lateral line (Haas and Gilmour, 2006; Lecaudey et al., 2008) and by the amoeba *Dictyostelium discoideum* (Hirose et al., 2011; Hayakawa et al., 2020). In addition, some clusters of epithelial cells were found to rotate 90° within an epithelial sheet during *Drosophila* eye development (Mlodzik, 1999; Mirkovic and Mlodzik, 2006; Jenny, 2010; Founounou et al., 2021). Although there are many possible explanations for such collective behavior (Haas and Gilmour, 2006; Lecaudey et al., 2008), it has been difficult to understand from a mechanistic standpoint, due to the many-body problem inherent in analyzing complex systems. In this regard, mechanical models are useful to better understand the forces that drive multi-cell behavior as noted in the Introduction, and the mechanism presented in this paper represents one possible explanation for such collective cell movement. By comparing experimental results, such as the spatial distribution of actomyosin and adhesion molecules in cells and observed cell shapes, with the results from our numerical simulations, we may uncover new insights into the complex patterns of cell movement observed in living systems.

Data availability statement

The original contributions presented in the study are included in the article/Supplementary Material, further inquiries can be directed to the corresponding author.

Author contributions

The author was the sole contributor of this work and approved the submitted version for publication.

Funding

This work was supported by a JSPS KAKENHI Grant Number JP20K03871, 23H04300 and 21H05310, the "Dynamic Alliance for Open Innovation Bridging Human, Environment and Materials" of the Ministry of Education, Culture, Sports, Science and Technology of Japan, and the Global Station for Soft Matter at Hokkaido University.

Acknowledgments

We would like to thank T. Nakagaki, H. Orihara, N. Nishigami, M. Nishikawa, M. Akiyama, M. Kimura, and Y. Tanaka for their valuable comments and discussions.

Conflict of interest

The author declares that the research was conducted in the absence of any commercial or financial relationships that could be construed as a potential conflict of interest.

Publisher's note

Supplementary material

The Supplementary Material for this article can be found online at: https://www.frontiersin.org/articles/10.3389/fcell.2023.1126819/full#supplementary-material

References

Aigouy, B., Farhadifar, R., Staple, D. B., Sagner, A., Röper, J. C., Jülicher, F., et al. (2010). Cell flow reorients the axis of planar polarity in the wing epithelium of Drosophila. *Cell.* 142(5), 773–786. doi:10.1016/j.cell.2010.07.042

Bächer, C., Khoromskaia, D., Salbreux, G., and Gekle, S. (2021). A three- dimensional numerical model of an active cell cortex in the viscous limit. *Front. Phys.* 9, 753230. doi:10.3389/fphy.2021.753230

Bergert, M., Chandradoss, S. D., Desai, R. A., and Paluch, E. (2012). Cell mechanics control rapid transitions between blebs and lamellipodia during migration. *Proc. Natl. Acad. Sci. U. S. A.* 109 (36), 14434–14439. doi:10.1073/pnas.1207968109

Bergert, M., Erzberger, A., Desai, R. A., Aspalter, I. M., Oates, A. C., Charras, G., et al. (2015). Force transmission during adhesion-independent migration. *Nat. Cell. Biol.* 17 (4), 524–529. doi:10.1038/ncb3134

Bodor, D. L., Pönisch, W., Endres, R. G., and Paluch, E. K. (2020). Of cell shapes and motion: The physical basis of animal cell migration. *Dev. Cell.* 52 (5), 550–562. doi:10.1016/j.devcel.2020.02.013

Bray, D., and White, J. G. (1988). Cortical flow in animal cells. *Science* 239 (4842), 883–888. doi:10.1126/science.3277283

Callan-Jones, A. C., and Voituriez, R. (2016). Actin flows in cell migration: From locomotion and polarity to trajectories. *Curr. Opin. Cell. Biol.* 38, 12–17. doi:10.1016/j.ceb.2016.01.003

Camley, B. A., Zhang, Y., Zhao, Y., Li, B., Ben-Jacob, E., Levine, H., et al. (2014). Polarity mechanisms such as contact inhibition of locomotion regulate persistent rotational motion of mammalian cells on micropatterns. *Proc. Natl. Acad. Sci. U. S. A.* 111 (41), 14770–14775. doi:10.1073/pnas.1414498111

Case, L. B., and Waterman, C. M. (2015)). Integration of actin dynamics and cell adhesion by a three-dimensional, mechanosensitive molecular clutch. *Nat. Cell. Biol.* 17 (8), 955–963. doi:10.1038/ncb3191

Farhadifar, R., Roper, J. C., Aigouy, B., Eaton, S., and Julicher, F. (2007). The influence of cell mechanics, cell-cell interactions, and proliferation on epithelial packing. *Curr. Biol.* 17, 2095–2104. doi:10.1016/j.cub.2007.11.049

Farutin, A., Étienne, J., Misbah, C., and Recho, P. (2019). Crawling in a fluid. *Phys. Rev. Lett.* 123 (11), 118101. doi:10.1103/PhysRevLett.123.118101

Fletcher, A. G., Osterfield, M., Baker, R. E., and Shvartsman, S. Y. (2014). Vertex models of epithelial morphogenesis. *Biophys. J.* 106, 2291–2304. doi:10.1016/j.bpj.2013.11.4498

Founounou, N., Farhadifar, R., Collu, G. M., Weber, U., Shelley, M. J., and Mlodzik, M. (2021). Tissue fluidity mediated by adherens junction dynamics promotes planar cell polarity-driven ommatidial rotation. *Nat. Commun.* 12 (1), 6974. doi:10.1038/s41467-021-27253-0

Friedl, P., and Gilmour, D. (2009). Collective cell migration in morphogenesis, regeneration and cancer. *Nat. Rev. Mol. Cel. Biol.* 10 (7), 445–457. doi:10.1038/nrm2720

Haas, P., and Gilmour, D. (2006)). Chemokine signaling mediates self-organizing tissue migration in the zebrafish lateral line. *Dev. Cell.* 10 (5), 673–680. doi:10.1016/j.devcel.2006.02.019

Haigo, S. L., and Bilder, D. (2011). Global tissue revolutions in a morphogenetic movement controlling elongation. *Science* 331 (6020), 1071–1074. doi:10.1126/science.1199424

Hayakawa, M., Hiraiwa, T., Wada, Y., Kuwayama, H., and Shibata, T. (2020). Polar pattern formation induced by contact following locomotion in a multicellular system. *Elife* 9, e53609. doi:10.7554/eLife.53609

Hirose, S., Benabentos, R., Ho, H. I., Kuspa, A., and Shaulsky, G. (2011). Self-recognition in social amoebae is mediated by allelic pairs of tiger genes. *Science* 333 (6041), 467–470. doi:10.1126/science.1203903

Innocenti, M. (2018). New insights into the formation and the function of lamellipodia and ruffles in mesenchymal cell migration. *Cell. Adh Migr.* 12 (5), 401–416. doi:10.1080/19336918.2018.1448352

Jankowiak, G., Peurichard, D., Reversat, A., Schmeiser, C., and Sixt, M. (2020). Modeling adhesion-independent cell migration. *Math. Models Methods Appl. Sci.* 30, 513–537. doi:10.1142/S021820252050013X

Jenny, A. (2010). Planar cell polarity signaling in the Drosophila eye. *Curr. Top. Dev. Biol.* 93, 189–227. doi:10.1016/B978-0-12-385044-7.00007-2

Kuwayama, H., and Ishida, S. (2013). Biological soliton in multicellular movement. *Sci. Rep.* 3, 2272. doi:10.1038/srep02272

Lämmermann, T., Bader, B. L., Monkley, S. J., Worbs, T., Wedlich-Söldner, R., Hirsch, K., et al. (2008). Rapid leukocyte migration by integrin-independent flowing and squeezing. *Nature* 453 (7191), 51–55. doi:10.1038/nature06887

Landau, L. D., and Lifshitz, E. M. (1976). "Mechanics," in *Course of theoretical physics*. 3rd edn. Volume 1 (Oxford: Butterworth- Heinemann).

Lecaudey, V., Cakan-Akdogan, G., Norton, W. H., and Gilmour, D. (2008). Dynamic Fgf signaling couples morphogenesis and migration in the zebrafish lateral line primordium. *Development* 135 (16), 2695–2705. doi:10.1242/dev.025981

Liu, Y. J., Le Berre, M., Lautenschlaeger, F., Maiuri, P., Callan-Jones, A., Heuzé, M., et al. (2015). Confinement and low adhesion induce fast amoeboid migration of slow mesenchymal cells. *Cell.* 160 (4), 659–672. doi:10.1016/j.cell.2015.01.007

Lo, C. M., Wang, H. B., Dembo, M., and Wang, Y. L. (2000). Cell movement is guided by the rigidity of the substrate. *Biophys. J.* 79 (1), 144–152. doi:10.1016/S0006-3495(00)76279-5

Mietke, A., Jülicher, F., and Sbalzarini, I. F. (2019). Self-organized shape dynamics of active surfaces. *Proc. Natl. Acad. Sci. U. S. A.* 116 (1), 29–34. doi:10.1073/pnas.1810896115

Mirkovic, I., and Mlodzik, M. (2006). Cooperative activities of drosophila DE-cadherin and DN-cadherin regulate the cell motility process of ommatidial rotation. *Development* 133 (17), 3283–3293. doi:10.1242/dev.02468

Mlodzik, M. (1999). Planar polarity in the Drosophila eye: A multifaceted view of signaling specificity and cross-talk. *EMBO J.* 18 (24), 6873–6879. doi:10.1093/emboj/18.24.6873

Montell, D. J., Yoon, W. H., and Starz-Gaiano, M. (2012)). Group choreography: Mechanisms orchestrating the collective movement of border cells. *Nat. Rev. Mol. Cell. Biol.* 13 (10), 631–645. doi:10.1038/nrm3433

Moure, A., and Gomez, H. (2020). Dual role of the nucleus in cell migration on planar substrates. *Biomech. Model. Mechanobiol.* 19 (5), 1491–1508. doi:10.1007/s10237-019-01283-6

O'Neill, P. R., Castillo-Badillo, J. A., Meshik, X., Kalyanaraman, V., Melgarejo, K., and Gautam, N. (2018). Membrane flow drives an adhesion-independent amoeboid cell migration mode. *Dev. Cell.* 46 (1), 9–22.e4. doi:10.1016/j.devcel.2018.05.029

Ohta, T., and Ohkuma, T. (2009). Deformable self-propelled particles. *Phys. Rev. Lett.* 102 (15), 154101. doi:10.1103/PhysRevLett.102.154101

Okuda, S., Sato, K., and Hiraiwa, T. (2022). Continuum modeling of non-conservative fluid membrane for simulating long-term cell dynamics. *Eur. Phys. J. E* 45, 69. doi:10.1140/epje/s10189-022-00223-0

Pagès, D. L., Dornier, E., de Seze, J., Gontran, E., Maitra, A., Maciejewski, A., et al. (2022). Cell clusters adopt a collective amoeboid mode of migration in confined nonadhesive environments. *Sci. Adv.* 8 (39), eabp8416. doi:10.1126/sciadv.abp8416

Paluch, E. K., and Raz, E. (2013). The role and regulation of blebs in cell migration. *Curr. Opin. Cell. Biol.* 25 (5), 582–590. doi:10.1016/j.ceb.2013.05.005

Rauzi, M., Verant, P., Lecuit, T., and Lenne, P. F. (2008). Nature and anisotropy of cortical forces orienting Drosophila tissue morphogenesis. *Nat. Cell. Biol.* 10, 1401–1410. doi:10.1038/ncb1798

Reversat, A., Gaertner, F., Merrin, J., Stopp, J., Tasciyan, S., Aguilera, J., et al. (2020). Cellular locomotion using environmental topography. *Nature* 582 (7813), 582–585. doi:10.1038/s41586-020-2283-z

Ruprecht, V., Wieser, S., Callan-Jones, A., Smutny, M., Morita, H., Sako, K., et al. (2015). Cortical contractility triggers a stochastic switch to fast amoeboid cell motility. *Cell.* 160 (4), 673–685. doi:10.1016/j.cell.2015.01.008

Sakamoto, R., Izri, Z., Shimamoto, Y., Miyazaki, M., and Maeda, Y. T. (2022). Geometric trade-off between contractile force and viscous drag determines the actomyosin-based motility of a cell-sized droplet. *Proc. Natl. Acad. Sci. U. S. A.* 119 (30), e2121147119. doi:10.1073/pnas.2121147119

Salbreux, G., Charras, G., and Paluch, E. (2012). Actin cortex mechanics and cellular morphogenesis. *Trends Cell. Biol.* 22 (10), 536–545. doi:10.1016/j.tcb.2012.07.001

Sato, K. (2017). Direction-dependent contraction forces on cell boundaries induce collective migration of epithelial cells within their sheet. *Dev. Growth Differ.* 59 (5), 317–328. doi:10.1111/dgd.12361

Sato, K., Hiraiwa, T., Maekawa, E., Isomura, A., Shibata, T., and Kuranaga, E. (2015). Left-right asymmetric cell intercalation drives directional collective cell movement in epithelial morphogenesis. *Nat. Commun.* 6, 10074. doi:10.1038/ncomms10074Refstyled

Sato, K., Hiraiwa, T., and Shibata, T. (2015). Cell chirality induces collective cell migration in epithelial sheets. *Phys. Rev. Lett.* 115, 188102. doi:10.1103/PhysRevLett.115.188102

Scarpa, E., and Mayor, R. (2016). Collective cell migration in development. *J. Cell. Biol.* 212 (2), 143–155. doi:10.1083/jcb.201508047

Taniguchi, A., Nishigami, Y., Kajiura-Kobayashi, H., Takao, D., Tamaoki, D., Nakagaki, T., et al. (2023). Light-sheet microscopy reveals dorsoventral asymmetric membrane dynamics of Amoeba proteus during pressure-driven locomotion. *Biol. Open* 12 (2), bio059671. doi:10.1242/bio.059671

Taniguchi, K., Maeda, R., Ando, T., Okumura, T., Nakazawa, N., Hatori, R., et al. (2011). Chirality in planar cell shape contributes to left-right asymmetric epithelial morphogenesis. *Science* 333 (6040), 339–341. doi:10.1126/science.1200940

Tee, Y. H., Shemesh, T., Thiagarajan, V., Hariadi, R. F., Anderson, K. L., Page, C., et al. (2015). Cellular chirality arising from the self-organization of the actin cytoskeleton. *Nat. Cell. Biol.* 17 (4), 445–457. doi:10.1038/ncb3137

Wan, L. Q., Chin, A. S., Worley, K. E., and Ray, P. (2016). Cell chirality: Emergence of asymmetry from cell culture. *Philos. Trans. R. Soc. Lond B Biol. Sci.* 371 (1710), 20150413. doi:10.1098/rstb.2015.0413

Weijer, C. J. (2009). Collective cell migration in development. *J. Cell. Sci.* 122 (Pt 18), 3215–3223. doi:10.1242/jcs.036517